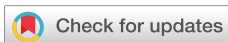


RESEARCH ARTICLE | NOVEMBER 22 2022

## Role of twin defects on growth dynamics and size distribution of undoped and Si-doped GaAs nanowires by selective area epitaxy

Daniel Ruhstorfer; Markus Döblinger; Hubert Riedl; Jonathan J. Finley ; Gregor Koblmüller 



*J. Appl. Phys.* 132, 204302 (2022)

<https://doi.org/10.1063/5.0124808>





### Instruments for Advanced Science

- Knowledge
- Experience
- Expertise

[Click to view our product catalogue](#)

Contact Hiden Analytical for further details:  
[www.HidenAnalytical.com](http://www.HidenAnalytical.com)  
[info@hiden.co.uk](mailto:info@hiden.co.uk)

Gas Analysis	Surface Science	Plasma Diagnostics	Vacuum Analysis
<ul style="list-style-type: none"><li>dynamic measurement of reaction gas streams</li><li>catalysis and thermal analysis</li><li>molecular beam studies</li><li>dissolved species probes</li><li>fermentation, environmental and ecological studies</li></ul>	<ul style="list-style-type: none"><li>UHV TPD</li><li>SIMS</li><li>end point detection in ion beam etch</li><li>elemental imaging - surface mapping</li></ul>	<ul style="list-style-type: none"><li>plasma source characterization</li><li>etch and deposition process reaction kinetic studies</li><li>analysis of neutral and radical species</li></ul>	<ul style="list-style-type: none"><li>partial pressure measurement and control of process gases</li><li>reactive sputter process control</li><li>vacuum diagnostics</li><li>vacuum coating process monitoring</li></ul>

# Role of twin defects on growth dynamics and size distribution of undoped and Si-doped GaAs nanowires by selective area epitaxy

Cite as: J. Appl. Phys. 132, 204302 (2022); doi: 10.1063/5.0124808

Submitted: 8 September 2022 · Accepted: 7 November 2022 ·

Published Online: 22 November 2022



Daniel Ruhstorfer,<sup>1</sup> Markus Döblinger,<sup>2</sup> Hubert Riedl,<sup>1</sup> Jonathan J. Finley,<sup>1</sup>  and Gregor Koblmüller<sup>1,a)</sup>

## AFFILIATIONS

<sup>1</sup>Walter Schottky Institute and Physics Department, Technical University of Munich, Garching, Germany

<sup>2</sup>Department of Chemistry, Ludwig-Maximilians-University Munich, Munich, Germany

<sup>a)</sup>Author to whom correspondence should be addressed: [Gregor.KoblmueLLer@wsi.tum.de](mailto:Gregor.KoblmueLLer@wsi.tum.de)

## ABSTRACT

We report the effects of Si doping on the growth dynamics and size distribution of entirely catalyst-free GaAs nanowire (NW) arrays grown by selective area molecular beam epitaxy on SiO<sub>2</sub>-masked Si (111) substrates. Surprising improvements in the NW-array uniformity are found with increasing Si doping, while the growth of undoped NWs appears in a metastable regime, evidenced by large size and shape distributions, and the simultaneous presence of crystallites with tetrahedral termination. Correlating scanning electron microscopy and transmission electron microscopy investigations, we propose that the size and shape distributions are strongly linked to the underlying twin defect formation probabilities that govern the growth. Under the present growth conditions, Si-doping of GaAs NWs leads to a very high twin defect formation probability (~0.4), while undoped NWs exhibit a nearly threefold decreased probability (~0.15). By adopting a model for facet-mediated growth, we describe how the altered twin formation probabilities impact the competing growth of the relevant low-index NW facets, and hence, NW size and shape. Our model is further supported by a generic Monte Carlo simulation approach to highlight the role of twin defects in reproducing the experimentally observed size distributions.

© 2022 Author(s). All article content, except where otherwise noted, is licensed under a Creative Commons Attribution (CC BY) license (<http://creativecommons.org/licenses/by/4.0/>). <https://doi.org/10.1063/5.0124808>

## I. INTRODUCTION

Group-III arsenide nanowire (NW) arrays grown with high uniformity and accurate doping control have enabled an impressive series of electronic and optoelectronic devices over the past decade, including high-performance vertical transistors,<sup>1</sup> NW-laser arrays<sup>2</sup> and micro-LEDs (light emitting diodes),<sup>3,4</sup> as well as compact NW-solar cells.<sup>5,6</sup> Such NW-array devices are primarily realized by selective area epitaxy (SAE) techniques, which allow precise lithographic control of location, geometry, and size of NW-arrays via full site-controlled growth. SAE growth also prevents from critical growth issues seen in traditional, i.e., Au-assisted vapor-liquid-solid (VLS) growth, which is plagued by morphological inhomogeneities,<sup>7</sup> difficulties in doping control,<sup>8</sup> contamination by Au-precipitates,<sup>9</sup> and phase segregation in ternary or multi-component alloy NWs.<sup>10,11</sup>

For GaAs-based NWs, SAE growth with remarkable homogeneity has been demonstrated in many early reports by metal-organic vapor phase epitaxy (MOVPE).<sup>3,12-16</sup> In these works,

several essential growth dynamic properties, such as shape formation and surface diffusion limited vertical and lateral growth rates, were investigated in great detail as a function of growth parameters,<sup>12,13,16</sup> SAE mask window opening size and pitch,<sup>12,13</sup> and substrate type<sup>12,13,17,18</sup> and orientation.<sup>19,20</sup> A key finding was that under typical MOVPE growth parameters (V/III ratio, temperature), tetrahedral GaAs crystals were thermodynamically most stable, while hexagonal shaped NWs appear to form only via the introduction of rotational twin defects along the growth axis.<sup>13,15,21</sup> As a result, catalyst-free GaAs NWs always exhibit very large twin defect densities. The straightforward doping control, particularly of Si dopants providing the much desired n-type conductivity in catalyst-free GaAs NWs, has also motivated SAE growth efforts to be extended to MBE (molecular beam epitaxy) methods.<sup>22</sup> Both for MOVPE and MBE-based studies, n-type carrier densities well into the 10<sup>18</sup> cm<sup>-3</sup> range were achieved, although higher doping densities induce strong self-compensation effects.<sup>22,23</sup> Despite much effort on

16 April 2024 11:17:15

understanding and controlling the electrical activity of Si dopants in catalyst-free GaAs NWs, there are hardly any investigations into the morphological and structural evolution under Si doping.

In this work, we elucidate the influences of Si doping on the growth dynamics of SAE-type, catalyst-free GaAs NW arrays on SiO<sub>2</sub>-masked Si (111) substrates grown by MBE. We show, in particular, strong dependencies of Si doping on the NW-array uniformity, and how these are linked to the presence and competition of different GaAs crystal shape distributions. Combining high-resolution scanning electron microscopy (SEM) and transmission electron microscopy (TEM), we propose that the different twin defect formation probabilities in undoped vs Si-doped GaAs NWs are key parameters governing the observed NW-array distributions. We also present a simple growth model using Monte Carlo simulation to illustrate the influences of different twin formation probabilities on the NW length and width distribution via different growth rate dependences of the participating NW facets.

## II. EXPERIMENTAL DETAILS

Growth experiments were performed in a Veeco Gen-II MBE system equipped with conventional effusion cells for group-III elements, a valved cracker cell supplying uncracked As<sub>4</sub>, and solid-source dopant cells for silicon (Si) and carbon (C). We used 2 in. Si (111) wafers as substrates coated with 20-nm thick thermally grown SiO<sub>2</sub>, which serves as a mask layer for the SAE growth. The SiO<sub>2</sub> mask was pre-patterned identically for all samples using electron beam lithography and reactive ion etching to create periodic mask opening arrays, with diameters  $d_0$  ranging between 20 and 100 nm and a pitch of 250 nm (unless otherwise noted). Prior to loading the as-patterned wafers to the MBE system, a short wet chemical etching step using buffered hydrofluoric (HF) acid was applied to establish a hydrogen-terminated Si (111) surface within the openings to prevent reoxidation.<sup>24</sup> After degassing the substrates, the growth procedure followed the same exact sequences as in our previous work.<sup>22,25</sup> Essentially, the substrate was first

ramped to 870 °C under a high As<sub>4</sub>-beam equivalent pressure (BEP =  $5.5 \times 10^{-5}$  mbar) which helps to stabilize a Si(111):As  $1 \times 1$  surface phase,<sup>26</sup> needed to obtain the growth of Si-doped GaAs NWs with high yield.

Growth of the Si-doped GaAs NWs was then initiated under the same As<sub>4</sub>-BEP by lowering the temperature to 630 °C and, simultaneously, opening the Ga and Si shutters. The growth time was 1 h and Ga- and As-fluxes, as calibrated in equivalent GaAs (100) growth rate units, were selected as 0.4 and 32.5 Å/s (unless otherwise noted), which translates to a V/III ratio of 81. We selected these conditions based on the previous optimization of the NW growth selectivity and aspect ratio, while a lower V/III ratio as well as a lower or higher growth temperature, yielded inferior growth quality (see the [supplementary material](#)). In the following, a Si-doping series is presented where the Si dopant flux was varied by the heating current (units of Amperes) of the thermal Si sublimation source. For example, a heating current of 13A refers to a Si-flux of  $\sim 1.6 \times 10^{12} \text{ cm}^{-2} \text{ s}^{-1}$  in our MBE system, and linear changes in current correspond to exponentially varying Si dopant flux.<sup>27,28</sup> The respective Si-dopant fluxes were also calibrated in terms of equivalent bulk Si doping concentration in planar GaAs (100) thin films at a growth rate of  $\sim 1 \mu\text{m/h}$  using secondary ion mass spectrometry (SIMS). Here, a change in Si-cell heating current from, e.g., 11–13 A corresponds to an increase in Si doping concentration from  $2.1 \times 10^{18} \text{ cm}^{-3}$  to  $1.4 \times 10^{19} \text{ cm}^{-3}$  (Ref. 28).

As-grown Si-doped GaAs NWs along with undoped GaAs NW reference samples were then analyzed in terms of their growth morphology, crystal shape, and NW length/diameter by field-emission scanning electron microscopy (FE-SEM) using an NVision 40 FIB-SEM (Carl Zeiss). All SEM images shown in this study were recorded at a tilt angle (bird-eye view) of 54°. The microstructure of selected NW samples was further characterized by high-resolution transmission electron microscopy (HR-TEM) and selected area electron diffraction (SAED) patterns in a FEI Titan Themis operating at 300 kV.

16 April 2024 11:17:15

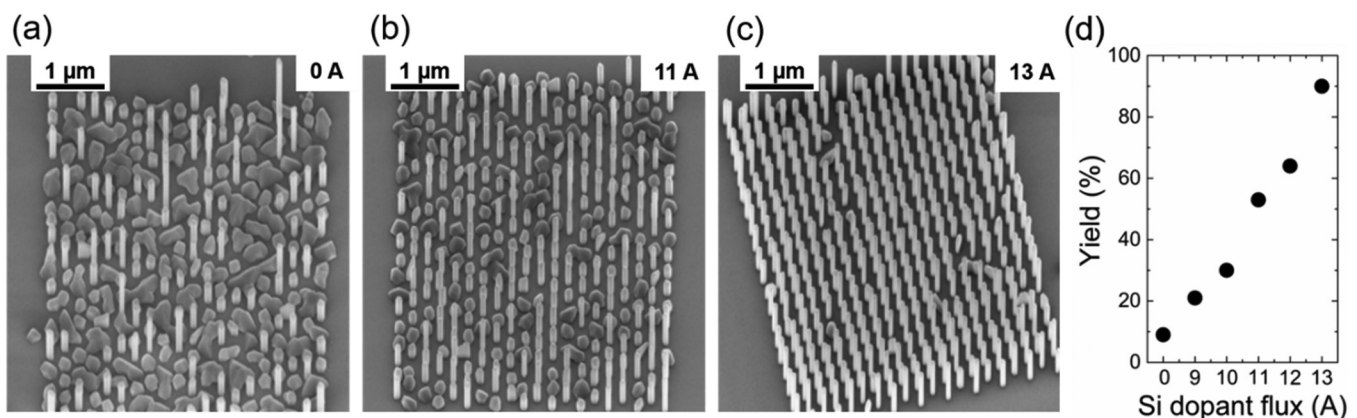


**FIG. 1.** (a)–(c) SEM micrographs of undoped (0A) and Si-doped (11A,13A) GaAs NWs as grown for 1 h, taken from an array with mask opening diameter of  $d_0 = 40$  nm. (d) The NW yield increases continually with Si dopant flux, showing very dynamic variation from ca. 10% (undoped case) to >90% under a very high Si dopant flux.

### III. RESULTS AND DISCUSSION

#### A. Nanowire growth yield in dependence of Si dopant flux

Figure 1 shows SEM micrographs of GaAs NW arrays ( $d_0 = 40$  nm) grown at different Si dopant fluxes, along with a plot summarizing the NW growth yield for each sample. We observe that growth without Si doping [Fig. 1(a)] results in only a relatively small fraction of distinct NWs ( $\sim 10\%$  yield), while GaAs crystallites of various shapes are the predominant features. Interestingly, with increasing Si dopant flux, the fraction of crystallites decreases whereas that of NWs increases continually, reaching a NW growth yield in excess of 90% for the highest Si dopant flux (13 A). To our knowledge, such dependence between doping and growth morphology/yield evolution has not yet been observed for any III-V semiconductor NWs—thus, developing an understanding for this behavior is one of the main objectives of this study. We note that similar bimodal shape distributions of NWs and crystallites within a single SAE-array were observed previously under other control parameters; however, without specific explanations. For example, Farrell *et al.* reported the simultaneous occurrence of pancake-like

crystals and NWs in high-periodicity SAE-arrays during InAsSb MOVPE growth, when using an increased mask opening diameter.<sup>29</sup> Similar characteristics were also found in the SAE-growth of InGaP, where the fraction of crystallites increased for wider mask openings at the expense of NWs.<sup>30</sup> Meta-stable growth regimes were also observed in the SAE growth of non-arsenide based III-V NWs, such as GaN NWs by MOVPE, yielding both pyramidal-shaped crystallites next to hexagonal-shaped NWs under  $H_2$  carrier gas.<sup>31</sup>

In our case of GaAs NWs, we emphasize that the preference for crystallites vs NWs stems directly from the dynamics during growth, rather than the underlying substrate surface or nucleation conditions, as we confirm by various experiments. First, we recognize that crystallite formation is not related to changes in growth selectivity of the SAE process, since growth takes place exclusively from the defined mask openings (100% selectivity, see also Fig. 2). Second, we performed two control experiments by which we modified the nucleation procedure of undoped and Si-doped GaAs NWs (see [supplementary material](#)). In the first experiment, GaAs NWs were nucleated without Si doping, followed by a long growth under high Si-dopant flux (13 A). This experiment yielded an excellent

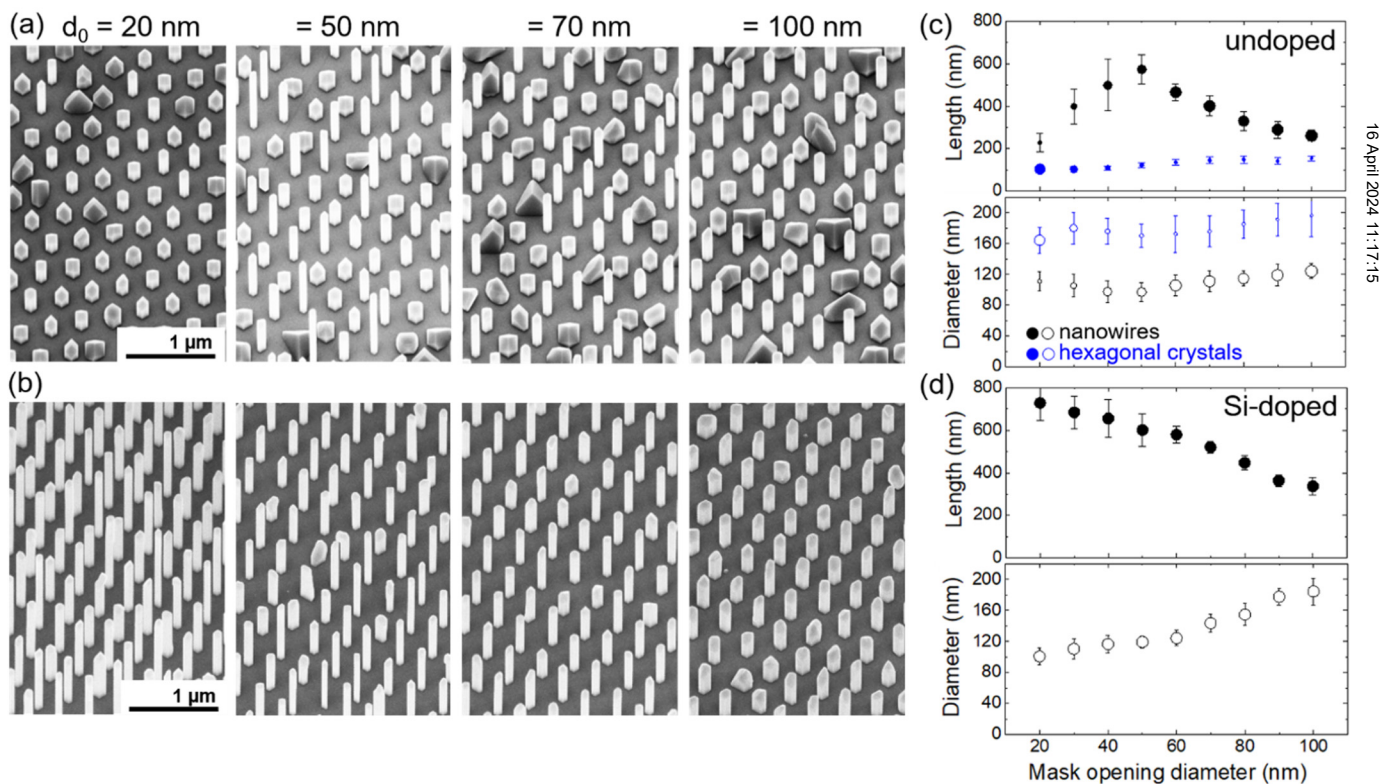


**FIG. 2.** SEM micrographs of (a) undoped (0A) and (b) Si-doped (13A) GaAs NW arrays obtained for different mask opening diameters  $d_0$ . (c) and (d) show plots of the corresponding length and diameter evolution as a function of  $d_0$  for the undoped (c) and Si-doped cases (d). Black and blue datapoints in (c) represent the bimodal distribution of composite NWs and hexagonal crystallites, respectively, and their relative proportions within the given array are reflected by the different sizes of datapoints [based on the analysis of Fig. 3(e)].

16 April 2024 11:17:15

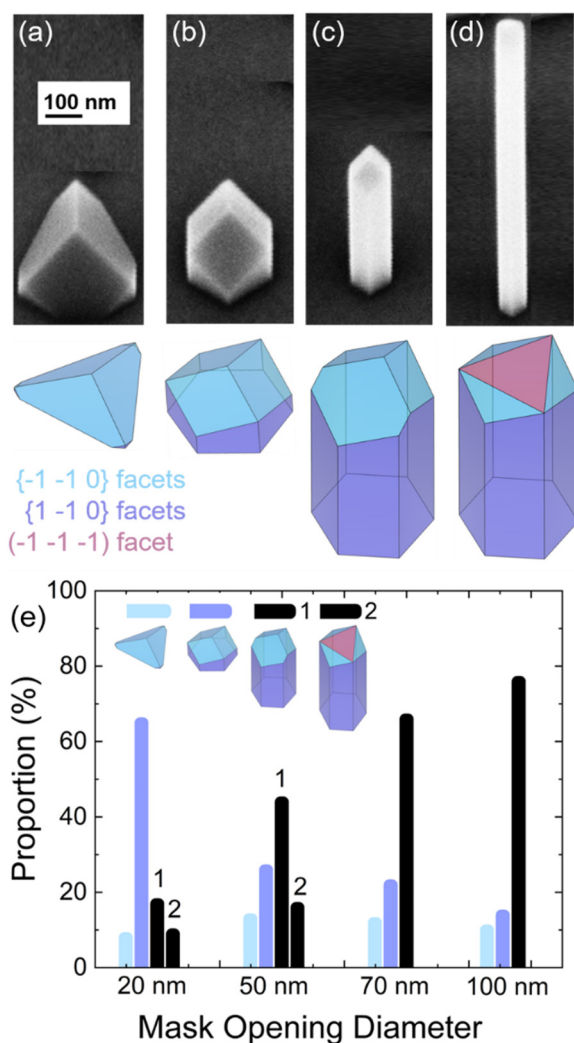


**FIG. 3.** Classification of the four characteristic crystal shapes observed in undoped GaAs NW arrays, illustrated by SEM micrographs (a)–(d) of isolated crystals (from an array with a wider pitch of 500 nm). Bottom panels depict schematics of the crystal shapes and corresponding facet structures; (a) tetrahedral crystallites terminated by  $\{1\bar{1}0\}$  crystal facets, (b) hexagonal crystallites with  $\{1\bar{1}0\}$ -type side facets and tilted  $\{1\bar{1}0\}$  facets forming a tetrahedra-shaped tip, (c) hexagonal NWs with low aspect ratio and facet structure similar to (b), and (d) high-aspect ratio hexagonal NWs that show a frequently truncated tetrahedral tip structure. (e) Histogram depicting the relative fractions of these crystal shapes for arrays with different mask opening diameters, as obtained by evaluating approx. 100 crystals per field. (1) and (2) correspond to low and high aspect-ratio NWs, respectively. For mask openings of 70 nm and 100 nm, no differentiation between these two types of NWs is made, and only their composite fraction is plotted.

growth yield of  $\sim 95\%$ , similar to Fig. 1(c). Inverting this sequence, by introducing a short nucleation step under high Si doping and then resuming growth without dopant supply, resulted in a very poor growth yield of  $\sim 15\%$ , similar to Fig. 1(a). Comparing these

results to the continuous growths shown in Fig. 1, clearly demonstrates that the yield of NWs is independent of the nucleation stage and that the distinction of whether nuclei develop into NWs or crystallites is determined by the presence or absence of Si dopants during growth.

## B. Nanowire and crystallite shapes and their dependencies on mask opening size

To illustrate more closely the evolution of NWs vs crystallites, Figs. 2 and 3 summarize their relative fractions and corresponding dimensions (length, diameter) as a function of the mask opening diameter  $d_0$ . We focus here specifically on a comparison of undoped NWs with the Si-doped NWs under the highest doping (13 A), to best capture the dynamics at the extreme ends of this series. For this comparison, we grew the NW arrays under slightly higher  $\text{As}_4$ -BEP of  $6 \times 10^{-5}$  mbar ( $V/\text{III} = 89$ ) and a growth time of 70 min, which provided an even better distinction between different crystallites and NWs, and their different shapes. From Figs. 2(b) and 2(d), it is evident that under high Si-doping only NWs are formed as predominant structures throughout all arrays, irrespective of the mask opening size. For all mask opening diameters  $d_0$ , the NW dimensions exceed the mask opening laterally. The NWs further exhibit a clear inverse length vs. diameter dependence, represented by increased NW length and decreased diameter at small  $d_0$ , and vice versa for larger  $d_0$ . This behavior is well observed by many previous SAE studies of GaAs NWs,<sup>12,13,18</sup> and reflects the group-III limited diffusion dynamics in catalyst-free NW arrays.

For undoped GaAs NWs, the trends are more complex: Here, a clear distinction between different crystallite and NW shapes needs to be made, and we classify four different shapes delineated in Fig. 3. First, tetrahedral crystallites with large lateral extension (yet, with a very low density) are observed, which are enclosed by three-fold symmetric  $\{1\bar{1}0\}$  crystal facets. Another class observed are crystallites which have developed a distinct hexagonal base (“hexagonal crystallites” with  $\{1\bar{1}0\}$ -type side facets) but are terminated immediately by symmetrically inclined  $\{1\bar{1}0\}$  facets (tetrahedra) on top. Note that the sidewall and inclined facets belong to the same family of planes, yet, we treat them separately to adhere to the conventional descriptions used in previous literature.<sup>13,21,32</sup> Finally, we categorize two different sets of NWs, seen especially in the limit of small mask opening size: on the one hand, NWs of a low aspect ratio (short length/wide diameter), with a well-defined hexagonal shape and a pronounced tetrahedra-shaped tip. These NWs appear to have the same facet structure as the short hexagonal crystallites. On the other hand, we also observe thinner NWs with a much increased aspect ratio and a less specific surface termination at the tip. These NWs, however, host either a faint tetrahedral tip structure or a more truncated tip structure, as verified by additional TEM analysis. As we further illustrate below, such truncated NW growth fronts are commonly associated with the development of distinct  $(111)\text{B}$  facets via the formation of twin defects in hexagonal NWs, and which promote the vertical growth of NWs.<sup>13,21,32</sup>

Sixfold symmetric hexagonal NWs and threefold symmetric tetrahedral crystallites were previously observed in MOVPE growth studies of undoped GaAs NWs, but their occurrence was not simultaneous and only selectively dependent on the respective growth

16 April 2024 11:17:15

conditions (temperature, V/III ratio).<sup>13,21</sup> In particular, tetrahedral crystallites were realized under decreased V/III ratio and increased growth temperature, while hexagon-shaped NWs were stabilized at decreased temperature and very high V/III ratio, since these conditions decreased the energy barrier difference between the two respective crystal shapes. Related work further noted that larger mask opening windows preferred the formation of hexagonal-shaped GaAs, while smaller windows resulted exclusively in tetrahedral-shaped crystallites.<sup>33</sup> These observations are, at least partly, also seen in our growth optimization runs (supplementary material), where only tetrahedral crystallites were found at a high temperature of 700 °C. However, for undoped GaAs NWs, no uniform NW arrays without the presence of crystallites are feasible, even when tuning growth over wide growth parameter windows (supplementary material). This suggests that MBE does not offer the wide tunability in growth kinetics as MOVPE, likely being limited by the accessible As-overpressure and V/III ratios.

As such, for MBE growth, only metastable growth regimes exist for undoped GaAs NWs while stabilization of relatively uniform NW arrays (without undesired crystallites) is facilitated by Si dopants. Hence, for undoped GaAs NWs, not only the typical hexagonal NWs and tetrahedra occur side by side under fixed growth conditions and fixed mask opening size, but also the existence of intermediate shapes (short hexagonal crystallites and NWs with distinct tetrahedral tips). Interestingly, the proportions of these different crystal shapes change with varying mask opening sizes. As depicted in Figs. 2(a) and 3(e), well-defined NW shapes with decent aspect ratios are observed for large  $d_0$ , i.e., constituting ~70%–80% of all crystals at  $d_0 = 70$ –100 nm. For such a large mask opening diameter, one can hardly differentiate though between the two NW-types since their size dispersion equilibrates due to the overall shorter NW length. Hence, the sum of all NWs, irrespective of their tip structure, is enclosed in the analysis. When decreasing  $d_0$  down to 20 nm, the distinction between the high aspect ratio NWs and low aspect ratio NWs (with their very distinct tetrahedral tips) becomes more apparent, and their overall fraction decreases at the expense of short hexagonal crystallites. Indeed, for  $d_0$  as low as 20 nm, the short hexagonal crystallites constitute the majority (~70%) of all observed crystal shapes. In contrast, the fraction of extended tetrahedral crystallites hardly changes with mask opening size, accounting to only ~10%.

Figure 2(c) plots the length and diameter of the most dominant crystal shapes as a function of mask opening size and further weighs their relative proportions by the size of datapoints as derived from the histograms of Fig. 3(e). Hence, in this analysis, we differentiate only between the size distributions of hexagonal crystallites (in blue) and the composite of all NW-types (in black). Quite different trends are observed with respect to the Si-doped GaAs NWs, evidenced by bimodal size distributions for undoped GaAs. Looking first at NWs, for small  $d_0$ , relatively short NWs are observed, which increase in length when  $d_0$  approaches ~50 nm. For  $d_0 > 50$  nm, the NW length decreases similar to the Si-doped case. Accordingly, the NW diameter exhibits an inverse trend, i.e., first a drop of diameter with  $d_0$  approaching ~50 nm, followed by an increase toward larger  $d_0$ . A somewhat similar, but much less pronounced trend in diameter dependence is also evident from the hexagonal crystallites, whereas their heights increase slightly with

$d_0$ . Finally, we note that short hexagonal crystallites are absent in the highly Si-doped samples, yet, different and uneven NW shapes (tetrahedral tips and truncated tips) are observed and contribute to the overall size dispersion within the arrays.

From these observations, we can hypothesize that in NW arrays with a large proportion of crystallites terminated with distinct tetrahedral tip structure (i.e., limit of small mask opening size  $d_0 = 20$ –50 nm) the growth of NWs shows a large propensity for early growth termination. Hence, NWs are on average much shorter as compared to Si-doped GaAs NWs in this regime, whereas for  $d_0 > 50$  nm, such differences in NW length are hardly noticeable between undoped and Si-doped NWs. In the following, we provide direct insights into these dynamic growth differences for undoped and Si-doped NWs by revealing distinct relationships with their underlying twin formation probabilities.

### C. Role of twin defects in the formation of undoped and Si-doped GaAs NWs

The shape evolution and stabilization of catalyst-free SAE-grown GaAs NWs is known to be strongly governed by twin defect formation, as hypothesized in an early work by Ikejiri *et al.*<sup>13</sup> and later confirmed in various other reports.<sup>15,21,32</sup> In fact, twin defects are quint-essential in the stabilization of hexagonal crystallite and NW shapes, such that NW growth of crystals with an underlying ZB-phase and without catalyst droplets is considered *only* possible via twin defects – coining the term “twin-induced growth mechanism.”<sup>13</sup> As further discussed below, the dynamics by which twin defects form in GaAs NWs depend on several dimensional and kinetic factors, which influence the competition of the participating growth facets. To describe these dynamics and establish links to the specific morphology evolution differences in undoped and Si-doped GaAs NWs, we performed a systematic twin defect analysis using TEM.

Figure 4 compares TEM micrographs and associated SAED (selected area electron diffraction) patterns of undoped (a)–(c) and Si-doped GaAs NWs (d) and (e), as extracted from identical growth fields with a mask opening diameter  $d_0 = 50$  nm. We selected NWs specifically from these growth fields, since the NW diameters for undoped and Si-doped GaAs NW are relatively similar, and hence, any variation in twin defect density directly reveals the effects by Si doping. The NWs depicted in the TEM micrographs have a diameter of 112 nm (undoped NWs) and 104 nm (Si-doped NWs), respectively. The SAED patterns of both NWs clearly evidence the underlying ZB-domain structure with twofold sets of reflections associated with the twin domains along the [111] orientation. We note that the individual reflections are more smeared out for the Si-doped NW, indicative of a more frequent stacking/twinning disorder. The different crystal orientations of the two respective twin domains are also reflected by the brightness contrast in the TEM images along the [111]B growth axis. A direct glance already shows that twin domain lengths are on average larger for the undoped NW in comparison to the Si-doped NW. High-resolution scanning TEM imaging allows a more quantitative assessment of the typical twin-domain segment lengths (denoted as ZB-A and ZB-B domains), and the corresponding twin defect densities. As illustrated in Fig. 4(a) for the undoped NW, the twin-free domain

16 April 2024 11:17:15

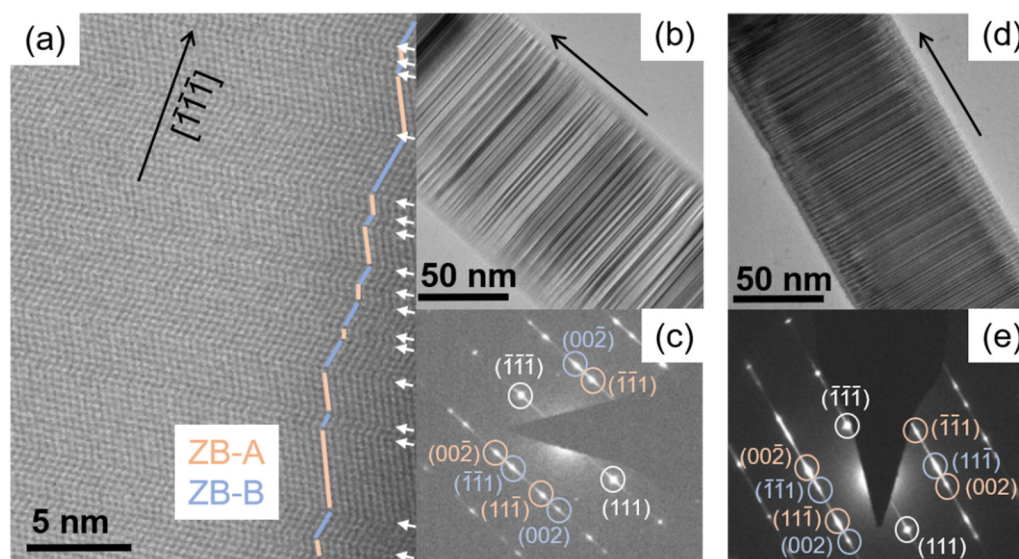


**FIG. 4.** TEM images and corresponding SAED patterns for undoped GaAs NW (a)–(c) and Si-doped GaAs NW (d) and (e). The high-resolution scanning TEM image as depicted in (a) shows the two different twin domains (ZB-A, ZB-B) by their alternating layer stacking orientation and the individual rotational twin defects marked by white arrows. The black arrow marks the growth orientation of the NW along  $[111]_B$ . The ZB-A and ZB-B twin domains are also represented in the SAED patterns by their respective color codes of the two sets of reflections.

length is typically between  $\sim 3$  and 13 GaAs bilayer wide, with a mean average of  $\sim 6$ –7 bilayers, as evaluated also in other regions. This corresponds to an average twin defect formation probability of 16%, which is given by the frequency of twins divided by the total number of GaAs bilayers. Twin formation probabilities of similar order (or even less) were also found previously in undoped GaAs NWs grown by MOVPE.<sup>15,21</sup> Analogous analysis performed on the Si-doped NW (see the [supplementary material](#)) resulted in an almost threefold increased twin formation probability as high as 41%. This means that a twin forms almost after every second GaAs bilayer, resulting in a very short-period twin domain structure. These results are consistent with the very recent data obtained for SAE-grown GaAsSb NWs, where twin defect densities were found to be  $\sim 3$  times higher in Si-doped NWs compared to undoped NWs—although twins were overall much less frequent due to the Sb surfactant effect.<sup>25</sup>

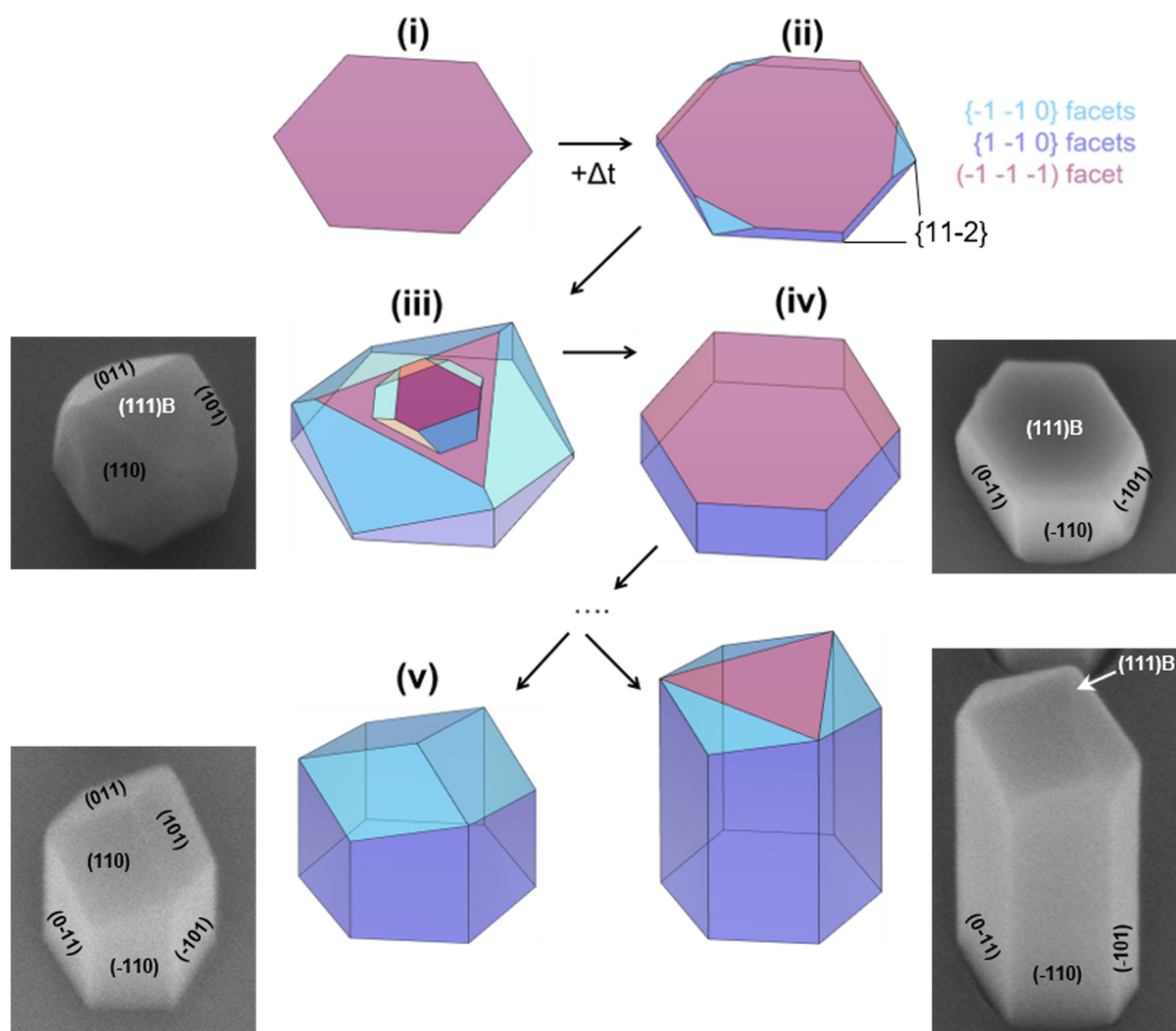
Another more qualitative difference between undoped and Si-doped NWs is found in the termination of the NW tip region and its relationship with twin defects. As shown in the [supplementary material](#), nearly all Si-doped NWs exhibit twin defect formation continuing to the very NW tip, irrespective of whether the tip is truncated by a flat  $(111)_B$  facet or a more uneven tetrahedra-like shape. For undoped NWs, we recognized that there are also several NWs with tips ending in a twin-free tetrahedral shape, similar to those found already in first generations of non-catalytic GaAs NWs grown by MBE.<sup>34</sup> This suggests that due to the lower twin formation probability seen in undoped NWs compared to Si-doped ones, these have a larger propensity for growth termination, once twins stopped forming.

#### D. Growth mechanisms describing different nanowire shapes

Based on these observations, we present in [Fig. 5](#) an intuitive growth model which describes the different shape evolutions and size dispersions found in the present NW arrays. The model aims to highlight specifically the relevant interplay in growth dynamics between the participating low-index growth facets and the driving mechanisms for twin formation. Hereby, we take previously proposed growth mechanisms for SAE-grown GaAs NWs into consideration,<sup>13</sup> and further support our description by showing realistic crystal shapes observed during growth via exemplary SEM images. Starting from a mask opening [stage (i)], nucleation of GaAs occurs first as thin extended mesas due to the increased lateral growth induced by surface diffusion of growth species via the  $\text{SiO}_2$  mask.<sup>13,21</sup> As pointed out by Ikejiri *et al.*,<sup>13</sup> the crystal shape that initially develops is a direct result of competing growth of the most relevant low-index facets, which are essentially the symmetric  $\{1-10\}$  side facets, the  $\{11-2\}$  facets pointing along the corners ( $30^\circ$ ), and the inclined  $\{-1-10\}$  facets intersecting with the  $(111)_B$  top facet. Facets will only appear when they are growing slowly, while fast growing facets terminate and disappear.

For conditions favoring NW growth (as mainly discussed here),  $\{1-10\}$  side facets grow slowly whereas  $\{11-2\}$  side facets grow out fast and terminate into corner facets, leading to the stabilization of a hexagonal base [stage (ii)]. Under dissimilar conditions (e.g., high growth temperature, see the [supplementary material](#)), inclined  $\{-1-10\}$  facets can actually exhibit the slowest growth rate over all other facets, and hence, the initial nuclei terminate into tetrahedral crystallites. This is not surprising, since the inclined

16 April 2024 11:17:15



16 April 2024 11:17:15

**FIG. 5.** Schematic illustration of GaAs NW shape evolution mediated by twin formation process, along with representative SEM images at different stages of growth. The color codes of the prevalent low-index facets are equivalent to those of Fig. 3, i.e.,  $\{1-10\}$  side-facets in purple, inclined  $\{-1-10\}$  facets in light blue, and  $(111)B$  top facet in pink. As shown for the final growth stage (v), NWs can terminate with tetrahedral tips when no new twins are formed (left) or continue to grow via the repeated introduction of new twins [triangular  $(111)B$  top facet] (right).

$\{-1-10\}$  facets have the same atomic configuration as the  $\{1-10\}$  side facets and are, therefore, expected to have an overall slow growth rate. This also means that under usual conditions favoring NW growth, the  $\{-1-10\}$  inclined facets are expected to become prominent as growth continues [see stage (iii), Fig. 5]. Hence, with growth proceeding along the vertical  $[111]B$  direction, the three inclined  $\{-1-10\}$  facets extend increasingly toward the center from the three corners where they emerge. This creates a flat triangle on the top  $(111)B$  facet [clearly visible in the corresponding SEM micrograph in Fig. 5, stage (iii)], because the top facet intersects

with the three inclined facets. The triangle continually shrinks as growth proceeds, and—in the worst-case scenario—terminates into a tetrahedral-shaped tip [see also stage (v), Fig. 5]. However, in the limit of a very small triangular top facet, the probability to form a rotational twin defect (rotating the stacking order by  $60^\circ$ ) in the next deposited layer is largely increased compared to the regular ZB stacking,<sup>13,21,52</sup> for energy minimization criteria discussed below and in Ref. 32. With the introduction of a rotational twin defect, however, on top of the original crystal lattice, new tilted  $\{-1-10\}$  facets are created that no longer present the slow growing

facets, but instead, turn into faster growing ones. This way, the twinned mesa formed on top grows out laterally, filling up the space above the original  $\{-1-10\}$  facets, which results in a NW with a flat extended (111)B top facet [see stage (iv) and SEM image in Fig. 5]. At this point, the new  $\{-1-10\}$  inclined facets will re-emerge in the consecutive growth, which are rotated by  $60^\circ$  with respect to the original  $\{-1-10\}$  facets below the twin defect. Thereby, the process illustrated in stage (iii) starts all over again, i.e.,  $\{-1-10\}$  inclined facets will extend, causing shrinkage of the top (111)B facet, until the next twin forms. This way, the NW grows vertically [see stage (v), Fig. 5] by piling up consecutive twins along the (111)B growth axis.

The rate at which successive twins form is obviously very different in undoped vs Si-doped GaAs NWs, with Si-doped GaAs NWs exhibiting much larger twin formation probabilities. The rate of twinning depends essentially on how quickly the limit of the small triangular (111)B top facet (critical size dimension) is reached by the growth of extended  $\{-1-10\}$  facets, as indicated above. As shown by previous work,<sup>32</sup> the size of the critical (111)B triangle is related to the change in Gibbs free energy for the growth of the next bilayer of the triangular area, which is governed by its surface energy density (areal and peripheral energy densities). In the limit of a small triangle, the lowered peripheral energy density of a rotated stacking makes it, thus, energetically more favorable for a twin to form. Hence, we believe that Si dopants must affect this peripheral/areal energy balance in a way that the critical dimension of the triangular (111)B top facet is enlarged as compared to the undoped case. Therefore, twin formation occurs much more readily, because it takes less growth to reach this critical triangle dimension when its size is large.<sup>32</sup> Microscopically, we suspect that a change in the surface structure due to Si dopants induces these changes in the anticipated surface energy balance, probably due to modifications in the surface reconstruction. Surface reconstructions such as the  $2 \times 2$  As-trimer based reconstruction are known to promote twin formation, as found in both planar (111)B GaAs epilayers<sup>35,36</sup> and NWs<sup>21</sup> alike. Si dopants may further develop complex reconstructions into non-polar (110)-like surfaces as reported for planar growth.<sup>37</sup> Yet, to what extent they modify the reconstructions on NWs needs detailed atomistic modeling as well as additional experimental efforts, e.g., scanning tunneling microscopy or x-ray photoemission spectroscopy studies.

Since the twin defects seen by TEM analysis are not equidistantly aligned along the growth axis, the twin defect formation probability obviously varies to some degree around its averaged value during the dynamic growth process. This is particularly prevalent for undoped GaAs NWs where the dynamic variations around the averaged twin formation probability ( $\sim 16\%$ ) are as large as  $\pm 8\%$ . We suspect that these variations may arise from any slight deviations from the perfectly symmetric crystal shape or small inhomogeneities in the adatom incorporation ratio during growth. This induces the likelihood that under such circumstances, the formation of new twins may be inhibited, as the extended  $\{-1-10\}$  facets terminate the growth by forming a tetrahedral tip. This is illustrated in stage (v) (Fig. 5) and shown also by the corresponding SEM image. Alternatively, with high chances of new twins forming during the shrinkage phase of the (111)B facet, NW growth can proceed and result not only in longer NWs (see SEM,

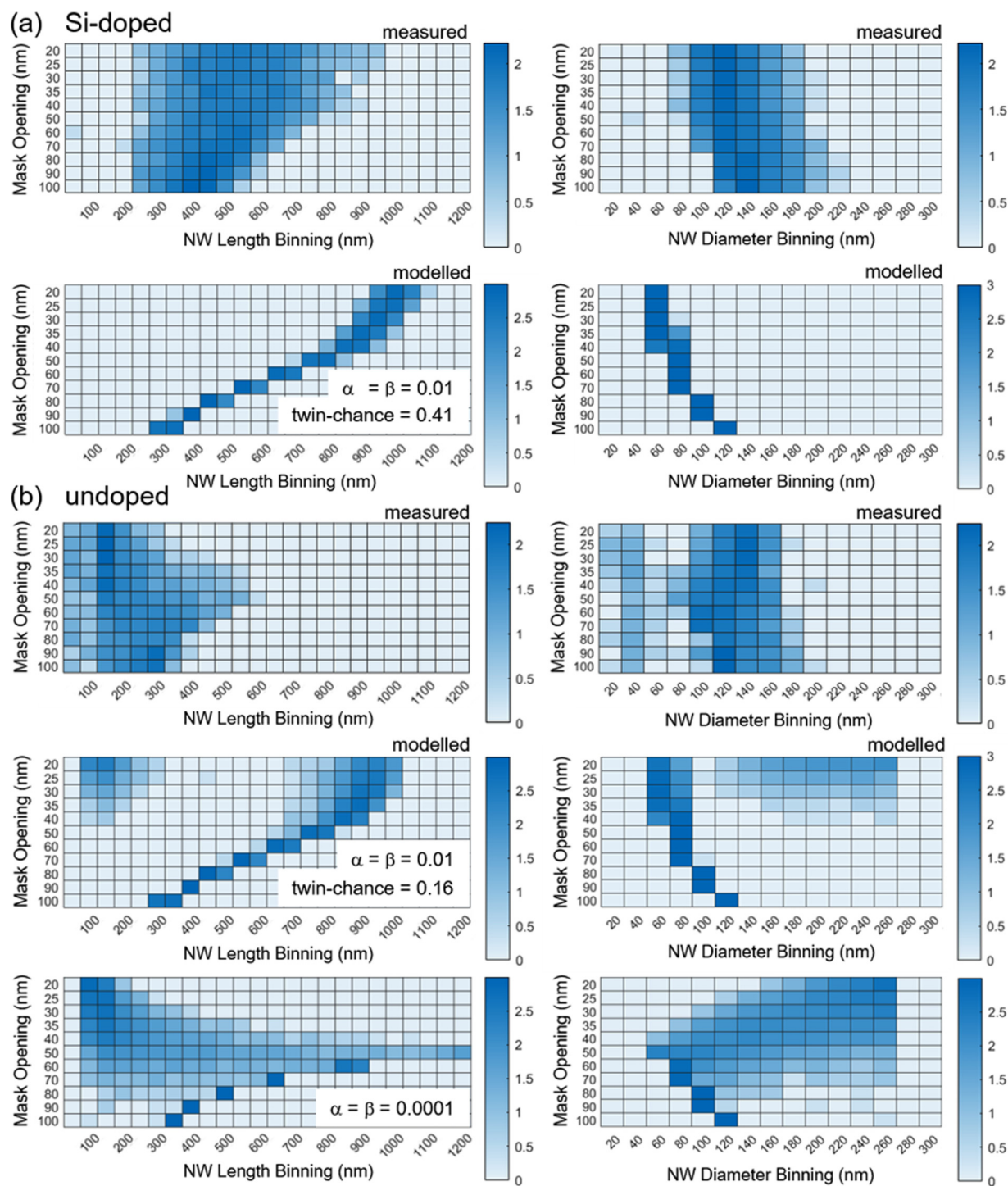
stage v, Fig. 5), but also in NWs with even tips terminated by a well-defined extended (111)B facet (see statistical TEM analysis in the supplementary material). Yao *et al.*<sup>32</sup> also argued that multiple consecutive twins could cause growth termination, especially when even numbers of twins emerge so close to each other that the twinned (111)B mesa cannot be stabilized. Moreover, variations in NW diameter are also known causes for different twin defect formation probabilities in GaAs NWs,<sup>15,21,32</sup> for the same reasons as stated above. As twin formation is governed by the size limit of the (111)B triangular top facet, it takes longer growth for a wider NW diameter to reach its critical dimension—hence, fewer twins are observed in thicker NWs. Such effects are, however, only observed for very large variations in NW diameter; e.g.,  $\sim 2$ -fold increase in NW diameter causes a factor of  $\sim 1.5$ – $2$  reduction in twin formation probability.<sup>15,21</sup> Much stronger changes in twin defect formation probability are commonly seen by tailoring growth parameters, especially via growth temperature (under fixed NW diameters).<sup>15,32</sup>

For our studied NWs, we can mostly rule out these effects, because, first of all, both the undoped and Si-doped GaAs NW arrays were grown under fixed conditions. Also, the comparative twin defect density study was performed on NWs from the same growth fields (mask opening size  $d_0 = 50$  nm), where the variation in NW diameter between the undoped and Si-doped NWs is negligible. For the undoped NWs, we further note that their diameter variation among different growth fields with variable mask opening size is also very small—e.g., only  $\sim 100$ – $120$  nm NW diameter variation in all undoped GaAs NWs arrays, see Fig. 2(c). Hence, we can assume that the twin formation probability is more or less constant throughout the undoped NW arrays, at least in the limit of sufficiently long growth as performed here. It is, therefore, quite interesting that we observe strong NW length variation and shape distribution for undoped GaAs NW arrays (especially for small mask opening sizes). We continue to describe this via growth modeling in the next section, and compare data with Si-doped GaAs NWs which underlie quite different twin formation probabilities.

## E. Modelling nanowire size distributions under different twin defect densities

In an attempt to interpret the NW size distributions, we propose a simple and generic nucleation-growth model (time-dependent Monte Carlo simulation) that captures the growth dynamics of the most relevant competing facets and the influences by twin formation at any given time during growth. Hereby, we start from an initial mask opening [e.g., a flat hexagonal opening, stage (i)] with a specific diameter  $d_0$ , and assume a constant material supply (volume  $V$ /time) throughout the growth process. As growth proceeds, i.e., every time an additional volume is added to the structure, a growth timer  $\Delta t$  is incremented in such a way that the growth rate remains constant—in other words, every NW is approximated by the same volume in the end. For a given time  $t$ , we then define a finite nucleation probability for the formation of a monolayer of GaAs on this hexagonal (111)B facet, as the areal fraction  $A_{(111)B}/(A_{(111)B} + \alpha \cdot A_{(-110)} + \beta \cdot A_{(-1-10)})$ . Here,  $A_{(111)B}$ ,  $A_{(-1-10)}$ , and  $A_{(-110)}$  stand for the respective surface areas of the different low-index facets, whereas  $\alpha$  and  $\beta$  describe nucleation probability parameters on the corresponding  $\{1-10\}$  and  $\{-1-10\}$

16 April 2024 11:17:15



16 April 2024 11:17:15

**FIG. 6.** Histograms illustrating NW length and diameter distribution as a function of mask opening size for (a) Si-doped and (b) undoped GaAs NW arrays. Top panels represent experimental data from SEM measurements of the same arrays as in Fig. 2, incorporating all observed features. Bottom panels show corresponding simulated data using the as-measured twin defect formation probabilities as fixed input parameters (41% for Si-doped NWs, 16% for undoped NWs), while  $\alpha, \beta$  are kept as free fitting parameters (see legends).

facets. These are expected to be very low ( $\alpha, \beta \ll 1$ ) since the  $\{1-10\}$  sidewall and  $\{-1-10\}$  inclined facets are, under typical NW growth conditions, very slow growing facets. In analogy, we also define similar nucleation probabilities for the  $\{1-10\}$  sidewall and  $\{-1-10\}$  inclined facets via  $\alpha \cdot A_{(1-10)} / (A_{(111)B} + \alpha \cdot A_{(-110)} + \beta \cdot A_{(-1-10)})$ , and  $\beta \cdot A_{(-1-10)} / (A_{(111)B} + \alpha \cdot A_{(-110)} + \beta \cdot A_{(-1-10)})$ , respectively. Now, as during growth stages (ii)–(iii) (Fig. 5) the nucleation probability on the (111)B facet succeeds along the growth direction, there is a finite probability for a twin to form (twin formation probability). When the growth time  $\Delta t$  reaches this limit for the nucleation of a twin, or when the (111)B facet disappeared entirely (forming a tetrahedral tip), a threshold is implemented which terminates the simulation. In the case of the complete disappearance of the (111)B facet (tetrahedral tip), the remaining growth time is then used to scale the NW structure accordingly. Likewise, when a twin is formed, the width is incrementally increased according to the lost volume growth rate, in order to fill the hexagonal prism from the twinned mesa [to reach stage (iv), Fig. 5]. The time  $\Delta t$  at which either the tetrahedral structure is terminated or the hexagonal prism reached, depends on the initial NW width, and hence, the mask opening size. As a result of this Monte Carlo simulation approach, the finite twin formation probability results in NW width and length variation due to the growth rate dependences on the area of the facets.

The resulting data are summarized in Fig. 6, comparing histograms of the modeled NW length and diameter distribution with the experimentally observed distributions for both the Si-doped case [Fig. 6(a)] and the undoped case [Fig. 6(b)]. Experimental data stem from the same NW arrays as depicted in Fig. 2, and incorporate all NW and crystallite features in the analysis here. The simulated data use the TEM-measured twin defect formation probabilities as input parameters (referred to also as twin-chance), and the only free fitting parameters are the nucleation probabilities  $\alpha, \beta$  ( $\ll 1$ ) for the slow-growing  $\{1-10\}$  sidewall and inclined  $\{-1-10\}$  facets. These parameters are essentially related to the surface free energies of these facets, since they represent the density of dangling bonds governing the nucleation probabilities. We keep  $\alpha$  and  $\beta$  generic in our modeling, because the surface energies under dynamic growth processes are difficult to estimate under the complex step structure and different surface reconstructions involved. However,  $\alpha$  and  $\beta$  are expected to be quasi-identical, as the  $\{1-10\}$  sidewall and inclined  $\{-1-10\}$  facets belong to the same family of planes, sharing the same atomic configuration.

Figure 6(a) shows the data for Si-doped GaAs NWs under the given twin defect formation probability = 0.41, and  $\alpha = \beta = 0.01$ . The observed trends of the experimental data are quite well reproduced by simulation, verifying the dependencies of increasing NW length/decreasing diameter with lowered mask opening size. Even the actual size dimensions obtained by simulation show reasonable agreement, e.g., modeled NW lengths are within 30% of the mean lengths measured by SEM while the NW diameters are slightly underestimated by the simulation. We note that changes of  $\alpha$  and  $\beta$ , especially toward smaller values, cause significant departure from this overall good agreement since NW lengths get unrealistically large. Using the same values for  $\alpha$  and  $\beta$ , but implementing the nearly 3-fold lower twin defect formation probability (0.16), we derive the respective NW size distributions

for undoped GaAs NWs shown in Fig. 6(b). Hypothetically, we also performed a simulation for further reduced twin defect formation probability (0.05, see the supplementary material) to demonstrate the prominent effect of twin defect density on NW size distribution. Interestingly, under the altered twin formation probability, we start observing an onset of bimodal size distribution in the range of small mask openings ( $d_0 = 20-50$  nm). Here, both long and short NWs appear [Fig. 6(b)], qualitatively similar to the experimental observations of NWs next to hexagonal crystallites seen in Fig. 2(c). Although for the given values of  $\alpha$  and  $\beta$ , the deviation in NW length dependence between modeled and experimental data is still fairly large. A significantly improved coincidence with the experimental size distribution can be achieved by adjusting the fitting parameters  $\alpha$  and  $\beta$  ( $= 0.0001$ ) as shown in the bottom panel of Fig. 6(b). Indeed, it is reasonable to assume that the nucleation probabilities ( $\alpha, \beta$ ) are not identical for Si-doped and undoped cases, as we expect modified surface-free energies under the presence (or absence) of dopants. Overall, this confirms that the simulation can directly capture the increased propensity for early growth termination, as expected from the increased proportion of NWs and crystallites terminating in tetrahedral tips (cf. Fig. 3). Obtaining an ultimate, comprehensive picture, which includes fully quantitative relationships between nucleation probability and surface free energies, requires detailed atomistic investigations of the relevant low-index surfaces during growth, their surface reconstructions, and Si-induced surface phase changes. This clearly motivates for future works and methods such as atom probe tomography, scanning tunneling microscopy, and density functional theory approaches to capture the characteristic atomistic differences of doped and undoped NW surfaces.

#### IV. CONCLUSIONS

We investigated the influence of Si doping on the growth kinetics and size distribution of catalyst-free GaAs NW arrays grown by selective area MBE processes on SiO<sub>2</sub>-masked Si (111) substrates. Undoped GaAs NWs were found to exhibit large size and shape distributions, including the presence of hexagonal and tetrahedral crystallites, indicative of metastable growth. In contrast, Si-doping resulted in significant improvements in NW-array uniformity and the absence of undesired crystallites. To further describe these dynamics, a growth model was developed for the evolution of specific morphologies and size distributions, highlighting the influence of different twin defect densities on these dynamics. Specifically, Si-doped GaAs NWs were found to exhibit much higher (~threefold) twin defect formation probabilities compared to undoped GaAs NWs, verified by high-resolution transmission electron microscopy. Based on the facet-mediated growth under the catalyst-free process, we illustrated how the different twin defect formation probabilities change the growth rate dependencies of the relevant low-index GaAs facets, explaining also the termination into tetrahedral NW facets. The observed NW size distributions were supported by Monte Carlo simulations, which reproduced the experimental data and further evidenced the occurrence of bimodal distributions seen in undoped GaAs NWs.

16 April 2024 11:17:15

## SUPPLEMENTARY MATERIAL

See the [supplementary material](#) for the growth optimization of undoped GaAs NWs, the nanowire yield dependence on different nucleation conditions, additional TEM micrographs of the NW tip region for undoped and Si-doped GaAs NWs, as well as of the twin domain structure of Si-doped NWs, and results from the modeling of NW size distributions at low twin defect densities.

## ACKNOWLEDGMENTS

We acknowledge financial support by the Deutsche Forschungsgemeinschaft (DFG, German Research Foundation) under Germany's Excellence Strategy via e-conversion, EXC No. 2089/1-390776260, the DFG-Project No. KO-4005/5-1, and the TUM International Graduate School of Science and Engineering (IGSSE).

## AUTHOR DECLARATIONS

## Conflict of Interest

The authors declare no conflict of interest.

## Author Contributions

**Daniel Ruhstorfer:** Conceptualization (equal); Data curation (equal); Formal analysis (equal); Investigation (equal); Methodology (equal). **Markus Döblinger:** Data curation (equal); Formal analysis (equal); Investigation (equal); Methodology (equal); Writing – review & editing (equal). **Hubert Riedl:** Methodology (equal); Resources (equal). **Jonathan J. Finley:** Resources (equal). **Gregor Koblmüller:** Conceptualization (equal); Data curation (equal); Formal analysis (equal); Funding acquisition (equal); Investigation (equal); Methodology (equal); Project administration (equal); Resources (equal); Software (equal); Supervision (equal); Validation (equal); Visualization (equal); Writing – original draft (equal); Writing – review & editing (equal).

## DATA AVAILABILITY

The data that support the findings of this study are available within the article and its [supplementary material](#).

## REFERENCES

- <sup>1</sup>K. Tomioka, M. Yoshimura, and T. Fukui, *Nature* **488**, 189 (2012).
- <sup>2</sup>H. Kim, W.-J. Lee, A. C. Farrell, J. S. D. Morales, P. Senanayake, S. V. Prihodko, T. J. Ochalski, and D. L. Huffaker, *Nano Lett.* **17**, 3465 (2017).
- <sup>3</sup>K. Tomioka, J. Motohisa, S. Hara, K. Hiruma, and T. Fukui, *Nano Lett.* **10**, 1639 (2010).
- <sup>4</sup>E. Dimakis, U. Jahn, M. Ramsteiner, A. Tahraoui, J. Grandal, X. Kong, O. Marquardt, A. Trampert, H. Riechert, and L. Geelhaar, *Nano Lett.* **14**, 2604 (2014).
- <sup>5</sup>I. Aberg, G. Vescovi, D. Asoli, U. Naseem, J. P. Gilboy, C. Sundvall, A. Dahlgren, K. E. Svensson, N. Anttu, M. T. Björk, and L. Samuelson, *IEEE J. Photovolt.* **6**, 185 (2016).
- <sup>6</sup>J. E. M. Haverkort, E. C. Garnett, and E. P. A. M. Bakkers, *Appl. Phys. Rev.* **5**, 031106 (2018).
- <sup>7</sup>M. C. Plante and R. R. LaPierre, *J. Cryst. Growth* **286**, 394 (2006).
- <sup>8</sup>W. Kim, L. Güniat, A. Fontcuberta i Morral, and V. Piazza, *Ann. Phys. Rev.* **8**, 011304 (2021).
- <sup>9</sup>D. E. Perea, J. E. Allen, S. J. May, B. W. Wessels, D. N. Seidman, and L. J. Lauhon, *Nano Lett.* **6**, 181 (2006).
- <sup>10</sup>Y.-N. Guo, H.-Y. Xu, G. J. Auchterlonie, T. Burgess, H. J. Joyce, Q. Gao, H. H. Tan, C. Jagadish, H.-B. Shu, X.-S. Chen, W. Lu, Y. Kim, and J. Zou, *Nano Lett.* **13**, 643 (2013).
- <sup>11</sup>G. Koblmüller and G. Abstreiter, *Phys. Stat. Sol. RRL* **8**, 11 (2014).
- <sup>12</sup>J. Noborisaka, J. Motohisa, and T. Fukui, *Appl. Phys. Lett.* **86**, 213102 (2005).
- <sup>13</sup>K. Ikejiri, T. Sato, H. Yoshida, K. Hiruma, J. Motohisa, S. Hara, and T. Fukui, *Nanotechnology* **19**, 265604 (2008).
- <sup>14</sup>A. C. Scofield, J. N. Shapiro, A. Lin, A. D. Williams, P.-S. Wong, B. L. Liang, and D. L. Huffaker, *Nano Lett.* **11**, 2242 (2011).
- <sup>15</sup>J. N. Shapiro, A. Lin, C. Ratsch, and D. L. Huffaker, *Nanotechnology* **24**, 475601 (2013).
- <sup>16</sup>K. P. Bassett, P. K. Mohseni, and X. Li, *Appl. Phys. Lett.* **106**, 133102 (2015).
- <sup>17</sup>K. Tomioka, Y. Kobayashi, J. Motohisa, S. Hara, and T. Fukui, *Nanotechnology* **20**, 145302 (2009).
- <sup>18</sup>H. Kim, D. Ren, A. C. Farrell, and D. L. Huffaker, *Nanotechnology* **29**, 085601 (2018).
- <sup>19</sup>K. Ikejiri, J. Noborisaka, S. Hara, J. Motohisa, and T. Fukui, *J. Cryst. Growth* **298**, 616 (2007).
- <sup>20</sup>Y. Minami, A. Yoshida, J. Motohisa, and K. Tomioka, *J. Cryst. Growth* **506**, 135 (2019).
- <sup>21</sup>H. Yoshida, K. Ikejiri, T. Sato, S. Hara, K. Hiruma, J. Motohisa, and T. Fukui, *J. Cryst. Growth* **312**, 52 (2009).
- <sup>22</sup>D. Ruhstorfer, S. Mejia, M. Ramsteiner, M. Döblinger, H. Riedl, J. J. Finley, and G. Koblmüller, *Appl. Phys. Lett.* **116**, 052101 (2020).
- <sup>23</sup>S. Arab, M. Yao, C. Zhou, P. D. Dapkus, and S. B. Cronin, *Appl. Phys. Lett.* **108**, 182106 (2016).
- <sup>24</sup>D. Ruhstorfer, A. Lang, S. Matich, M. Döblinger, H. Riedl, J. J. Finley, and G. Koblmüller, *Nanotechnology* **32**, 135604 (2021).
- <sup>25</sup>A. Ajay, H. Jeong, T. Schreitmüller, M. Döblinger, D. Ruhstorfer, N. Mukhundhan, P. Koolen, J. J. Finley, and G. Koblmüller, *Appl. Phys. Lett.* **121**, 072107 (2022).
- <sup>26</sup>M. A. Olmstead, R. D. Bringans, R. I. G. Uhrberg, and R. Z. Bachrach, *Phys. Rev. B* **34**, 6041 (1986).
- <sup>27</sup>J. Dufouleur, C. Colombo, T. Garma, B. Ketterer, E. Uccelli, M. Nicotra, and A. Fontcuberta i Morral, *Nano Lett.* **10**, 1734 (2010).
- <sup>28</sup>J. Becker, M. O. Hill, M. Sonner, J. Treu, M. Döblinger, A. Hirler, H. Riedl, J. J. Finley, L. J. Lauhon, and G. Koblmüller, *ACS Nano* **12**, 1603 (2018).
- <sup>29</sup>A. C. Farrell, W.-J. Lee, P. Senanayake, M. A. Haddad, S. V. Prihodko, and D. L. Huffaker, *Nano Lett.* **15**, 6614 (2015).
- <sup>30</sup>A. Berg, P. Caroff, N. Shahid, M. N. Lockrey, X. Yuan, M. T. Borgström, H. H. Tan, and C. Jagadish, *Nano Res.* **10**, 672 (2017).
- <sup>31</sup>S.-Y. Bae, J.-Y. Lee, J.-H. Min, and D. S. Lee, *Appl. Phys. Exp.* **6**, 075501 (2013).
- <sup>32</sup>M. Yao, C. Sheng, M. Ge, C.-Y. Chi, S. Cong, A. Nakano, P. D. Dapkus, and C. Zhou, *ACS Nano* **10**, 2424 (2016).
- <sup>33</sup>S. Ando, N. Kobayashi, and H. Ando, *J. Cryst. Growth* **145**, 302 (1994).
- <sup>34</sup>D. Rudolph, S. Hertenberger, S. Bolte, W. Paosangthong, D. Spirkoska, M. Döblinger, M. Bichler, J. J. Finley, G. Abstreiter, and G. Koblmüller, *Nano Lett.* **11**, 3848 (2011).
- <sup>35</sup>A. Y. Cho, *J. Appl. Phys.* **41**, 2780 (1970).
- <sup>36</sup>P. Chen, K. C. Rajkumar, and A. Madhukar, *Appl. Phys. Lett.* **58**, 1771 (1991).
- <sup>37</sup>W. I. Wang, E. E. Mendez, T. S. Kuan, and L. Esaki, *Appl. Phys. Lett.* **47**, 826 (1985).